Discrete linear local eigenmodes in a separating laminar boundary layer

Olaf Marxen†, Matthias Lang‡ and Ulrich Rist

Institut für Aerodynamik und Gasdynamik, Universität Stuttgart, Pfaffenwaldring 21,
D-70550 Stuttgart, Germany

The evolution of two- and three-dimensional small-amplitude disturbances in the laminar part of a laminar separation bubble is investigated in detail. We apply a combination of local linear stability theory, results from different experimental measurement campaigns and direct numerical simulations to identify two different discrete eigenmodes in the laminar part of the bubble. A stable eigenmode, the outer mode, governs unsteady oscillations in the upstream part of the bubble. However, this perturbation is quickly overtaken by an unstable eigenmode, the inner mode, which eventually leads to transition of the detached shear layer. Such a behaviour is observed due to an acceleration region with a favourable pressure gradient preceding the adverse-pressure-gradient region. The flow is stable in the acceleration region, in which the outer mode is only moderately damped, while the inner mode is strongly damped. At the onset of instability for the unstable eigenmode upstream of separation, both viscous Tollmien–Schlichting and inviscid Kelvin–Helmholtz instability mechanisms contribute to amplification, while deeper inside the bubble only the inviscid mechanism is active. If the explicit forcing is moved to a region downstream of the favourable pressure gradient, only the unstable eigenmode appears. The same behaviour is found for two-dimensional and weakly oblique waves.

1. Introduction

A laminar separation bubble (LSB) can originate if an initially laminar boundary layer is subject to a sufficiently strong adverse pressure gradient (APG) and detaches from the wall. In such a pressure-induced LSB, for example on an aerodynamic body such as a laminar aerofoil, laminar–turbulent transition occurs in the detached shear layer. If the body hosting the separated flow extents sufficiently far downstream, the turbulent flow reattaches eventually, and a closed bubble is formed. A comprehensive introduction to laminar separation bubbles, including a list of their characteristic features, is given in Marxen & Henningson (2011).

† Present address: Aeronautics and Aerospace Department, von Kármán Institute for Fluid Dynamics, Chaussée de Waterloo, 72, B-1640 Rhode-St-Genèse, Belgium. Email address for correspondence: olaf.marxen@vki.ac.be

‡ Present address: GE Global Research, Freisinger Landstrasse 50, 85748 Garching b. München, Germany.

Pressure-induced LSBs may occur on the surface of slender bodies, such as aerofoils, at low Reynolds numbers (Jones, Sandberg & Sandham 2008; Hain, Kähler & Radespiel 2009; Yarusevych, Sullivan & Kawall 2009). They often strongly affect aerofoil performance, mainly lift and drag. Gaster (1967) investigated pressure-induced LSBs on a flat plate in order to be able to vary Reynolds number and pressure distribution. This allowed him to produce a pressure distribution similar to 'the suction peak around the nose of a thin aerofoil at incidence' (p. 820). Here, we follow Gaster (1967)'s approach and investigate LSBs on a flat plate.

1.1. *Linear instability of unsteady waves in a separating boundary layer*

Several investigations of small-amplitude travelling waves in a separating boundary layer have lead to the now widely accepted view that these waves are amplified due to a viscous Tollmien–Schlichting (TS) mechanism (Tollmien 1929; Schlichting 1933) first, i.e. in the attached boundary layer upstream of the bubble and in the early laminar part of the LSB, followed by an inviscid Kelvin–Helmholtz (KH) instability mechanism. LSBs are very sensitive to triggering the KH instability via an explicit forcing of small-amplitude, convectively amplified perturbation waves (Kotapati *et al.* 2010; Marxen & Rist 2010; Marxen & Henningson 2011). These waves precede vortex formation.

Gruber, Bestek & Fasel (1987) were among the first to investigate the evolution of a Tollmien–Schlichting wave that enters a very small laminar separation bubble. The importance of Tollmien–Schlichting waves entering an LSB was later confirmed for larger, but still short, LSBs in several numerical, theoretical, and experimental investigations. In the numerical investigations of Maucher, Rist & Wagner (2000), instability waves were weakly amplified far ahead of the laminar separation bubble (cf. their figure 5) due to a viscous TS mechanism, before the flow separates and much stronger amplification of these instability waves occurs. In their experimental investigation, Häggmark, Bakchinov & Alfredsson (2000) found that 'close to the disturbance source the instability wave resembles a Tollmien–Schlichting wave', but that 'the amplitude distribution of the instability wave changes shape' upon entering the separated region. Similarly, Marxen *et al.* (2003) reported that 'the first section of the LSB is dominated by a primary convective instability of the two-dimensional TS-wave', while further downstream the instability wave assumes a shape 'characteristic for an inviscid free shear-layer type instability (so-called Kelvin–Helmholtz instability)'. For their LSB, Roberts & Yaras (2006) found that 'the T-S waves, at the very least, appear to provide the initial disturbances for transition to occur through the K–H mechanism'. Finally, Diwan & Ramesh (2009) came to the same conclusion in that 'the inviscid inflectional instability associated with the separated shear layer should be logically seen as an extension of the instability of the upstream attached adverse-pressure-gradient boundary layer', and hence could again fully confirm this traditional view.

The switchover between two different instability mechanisms, i.e. the TS and the KH, is a gradual process. Nevertheless, researchers have often associated these two mechanisms with different 'modes'. Rist & Maucher (2002) stated 'that an inviscid free shear layer type instability can be distinguished from a viscous wall-mode instability'. They used the 'the position and the relative strength of the eigenfunction maxima' to separate the two types of instabilities. Diwan & Ramesh (2009) also distinguished between two different modes: a 'wall mode of instability (i.e. TS mechanism)' and an 'inflectional (inviscid) mode'. The expression 'mode', however, may be confusing, as it is not always clear whether it refers to a certain type

of instability or to a mathematical eigenmode. The statement of Diwan & Ramesh (2009) that 'the Orr–Sommerfeld equation yields both inflectional (inviscid) and wall (viscous) modes' may imply that these are two separate mathematical eigenmodes, but no evidence in favour or against such a conjecture was presented in their paper.

The situation hence resembles that of supersonic flows, where two different instability mechanisms are active at a sufficiently high Mach number: a viscous (TS) instability and an acoustic (Mack) instability (Mack 1975). These may or may not correspond to two mathematical eigenmodes as discussed in Fedorov & Tumin (2011). Yet another similar situation can be observed for wall jets (Tumin & Aizatulin 1997; Levin *et al.* 2005), where an inner (wall) and an outer (shear layer) mathematical eigenmode can be found. In this paper, we will therefore investigate whether more than one mathematical eigenmode plays a role in an LSB. We will also determine the relation of eigenmode(s) to the two different instability mechanisms.

The traditional view that a Tollmien–Schlichting instability is followed by a Kelvin–Helmholtz instability as described above has been mostly observed for setups in which the boundary layer was not, or only mildly, accelerated before being decelerated in the APG region. However, in a flow in which the APG is preceded by a strong favourable pressure gradient, disturbances often decay even downstream of the separation point. Examples can be found in figure 9 of Watmuff (1999), in figure 13 of Lang, Rist & Wagner (2004), in figure 6 of Roberts & Yaras (2006), as well as in figure 16 of Postl, Balzer & Fasel (2011). In all these cases disturbances decay, or growth is much lower than predicted by linear stability theory (LST). Nevertheless, a Kelvin–Helmholtz-type instability is eventually observed. However, the decay of disturbances inside the separation region seemingly contradicts the traditional view described above. An explanation for this peculiarity has not yet been provided in the peer-reviewed literature. In this paper we will suggest one possible explanation for the decay of perturbations in the laminar part of an LSB.

The last point that will be addressed here is the occurrence of a linear instability for weakly oblique waves. These play a role in LSBs and have been investigated for the so-called oblique breakdown (Marxen & Rist 2010; Marxen & Henningson 2011), but an explicit comparison between LST, measurements and direct numerical simulations (DNS) has rarely been reported for LSBs. We will therefore analyse whether linear, amplified oblique waves can be observed experimentally in an LSB.

A number of considerations motivates our investigation of the linear disturbance stage in a separation bubble. Identifying the relevant disturbances and understanding their role in the vortex-formation and vortex-breakup process occurring further downstream is necessary to determine the number and kind of parameters influencing this process. This may aid in the interpretation of measurements and in implementing flow-control schemes such as the one used in Rist & Augustin (2006). Moreover, correctly capturing this stage of transition is believed to be a necessary condition for a simulation of (very) late stages with their complex interactions among different disturbances. Finally, we expect that simple models of the flow with an LSB, such as the one used by Sandham (2008), can be improved with better knowledge of the physical processes involved.

1.2. *Related work and outline*

The investigations of Marxen *et al.* (2003), Lang *et al.* (2004), Marxen, Rist & Wagner (2004) and Marxen *et al.* (2009) are based on the same flow field used here. Lang *et al.* (2004) report a comparison of results from different measurement techniques, including particle image velocimetry (PIV), with LST and DNS.

Marxen *et al.* (2003) give a short overview of the several features of transition in this flow field. Marxen *et al.* (2004) studied the effect of steady three-dimensional linear disturbances on the overall transition process, whereas Marxen *et al.* (2009) investigated growth mechanisms for this type of perturbation in the laminar part of the LSB. Here we specifically focus on unsteady perturbations preceding vortex formation.

After a description of the physical model and its mathematical formulation as well as the experimental setup in § 2, the mean flow will be described in § 3, including a linear stability analysis based on the Orr–Sommerfeld equation. An investigation of the growth of unsteady disturbances in the LSB (§ 4) considers the linear evolution of unsteady two- and three-dimensional disturbances. The paper closes with a summary and gives the main conclusions in § 5.

2. Physical model, experimental setup and mathematical formulation

A comparison of results from DNS and experimental methods serves to identify linear eigenmodes in a laminar separation bubble. These modes precede the laminar–turbulent transition. In addition, LST complements the set of tools used here. The key benefit of such a combined approach, reaching beyond a mere validation of the numerical or experimental method, comes from allowing us to determine the modal character of perturbations found in the boundary layer. For example, in DNS the location and size of the disturbance strip could easily be varied, which allowed us to specifically trigger different eigenmodes. Then, theoretical results aid in the interpretation of physical processes. LST assumes parallel flow, while the separating boundary-layer flow investigated here is not exactly parallel to the wall. However, the separation bubble is still fairly shallow, and previous investigations (see for example Marxen & Rist 2010; Marxen & Henningson 2011) have observed that LST works well for LSBs. Experimental data show which of the different possible disturbance states are realizable in the laboratory and may therefore be particularly relevant.

2.1. *Experimental setup and measurement techniques*

2.1.1. *Description of the setup and measurement campaigns*

The experimental setup is depicted in figure 1. Variants of such a setup have been used by other researchers before, for instance by Gaster (1967) and Watmuff (1999). Only a brief description of our specific setup will be given here; additional details can be found in Lang *et al.* (2004). A Cartesian reference system $(\breve{x}, \breve{y}, \breve{z})$, as shown in figure 1, constitutes the basic reference system throughout this work (dimensional quantities are marked by $\breve{}$). A velocity vector is denoted as $\boldsymbol{v} = [u, v, w]^{\mathrm{T}}$.

A flat plate is mounted in the free stream (free-stream velocity $\breve{U}_\infty = 0.125$ m s^{-1}) of the test section of a laminar water tunnel (kinematic viscosity $\nu_{water} \approx 10^{-6}$ m^2 s^{-1}). The turbulence intensity in the test section of the tunnel was $Tu \leqslant 0.05\,\%$ for 0.1–10 Hz. A streamwise pressure gradient is imposed locally on the flat-plate boundary layer by a triangular-shaped displacement body with a length $\breve{L}_{DB}^{Exp} = 0.69$ m. The resulting pressure distribution changes downstream from a strongly favourable pressure gradient (FPG) to a strongly adverse pressure gradient. This is a typical situation for boundary layers that occur on aerofoils at an angle of attack, as can be seen for instance in figure 12 of Jones *et al.* (2008). In the region of APG (starting at $\breve{x} \approx 0$ m), an LSB develops. The reference length is chosen to be $\breve{L}_{ref}^{Exp} = 2/3$ m $\approx \breve{L}_{DB}^{Exp}$. The reference velocity (for its derivation see Marxen 2005) is selected to be $\breve{U}_{ref}^{Exp} = 0.151$ m s^{-1} $\approx 1.2 \breve{U}_\infty$, resulting in a Reynolds number $Re_{global} = \breve{U}_{ref}^{Exp} \breve{L}_{ref}^{Exp} / \breve{\nu} = 10^5$.
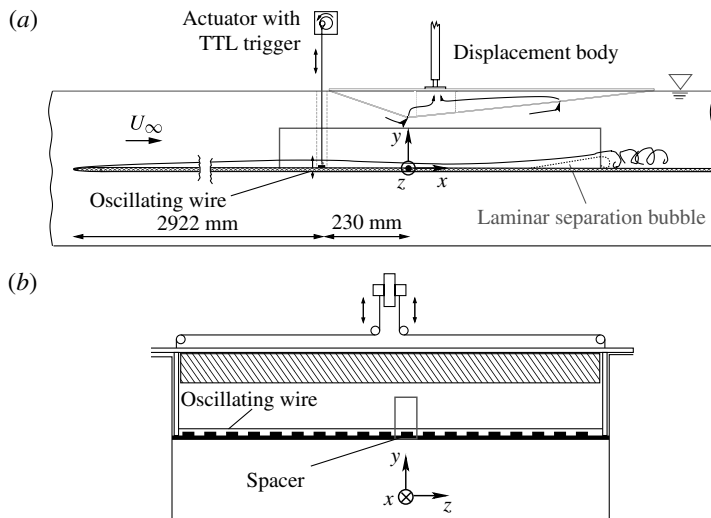
FIGURE 1. Sketch of the test section of the laminar water tunnel. The integration domain used for DNS case D_{LDE} is indicated by a box (not to scale). (*a*) Side view and (*b*) front view.

The minimum distance between the flat plate and the displacement body is $y = 0.15$.

The setup has been used for several measurement campaigns carried out at the Institut für Aerodynamik und Gasdynamik (IAG), Universität Stuttgart. Velocity data have been collected by means of laser-Doppler anemometry (LDA) and PIV. LDA measurements have been repeated and the resulting two different data sets are referred to by the respective year in which the data were collected, i.e. LDA (2000) and LDA (2001).

2.1.2. *Disturbance forcing in the experiment*

To ensure reproducible results that are independent of this particular water tunnel and its background noise in the relevant frequency range, it is desirable to have explicit control over the disturbances present in the flow. Following a classic approach in transition research (Klebanoff, Tidstrom & Sargent 1962; Kachanov & Levchenko 1984), this is achieved by forcing disturbances explicitly.

A two-dimensional time-harmonic disturbance is introduced upstream of the displacement body at $\check{x} = -0.23$ m ($x = -0.345$) by an oscillating wire of frequency $\check{f}_0 = 1.1$ Hz. Additionally, three-dimensional disturbances are imposed by placing thin (height 10^{-3} m) rectangular metal plates (denoted below as 'spacer' or 'spacers') regularly underneath the wire (figure 1). The spanwise distance between the spacers sets the fundamental spanwise wavelength $\check{\lambda}_z = 0.058$ m ($\lambda_z = 0.087$). The spanwise wavelength was selected experimentally through flow visualizations (Lang *et al.* 2004). Marxen, Rist & Henningson (2006) describe that 'in the experiment, the wave length ... was varied until the most regular vortical structures appeared'. LDA data were phase-averaged using a trigger signal generated by the actuator driving the wire (Lang *et al.* 2004). The only difference between the setup in cases LDA (2000) and LDA (2001) lies in the wall-normal position of the oscillating wire, which is $y = 4.2$ mm in case LDA (2000) and $y = 3.4$ mm in LDA (2001), resulting in minor differences in the amplitudes of forced disturbances.

Re_{global}	γ_0	x_{ifl}	x_{ofl}	y_{max}	$x_{o,usable}$
10^5	72	-0.6	0.6175	0.1207	0.41

TABLE 1. Computational parameters for the numerical test case D_{LDE}.

2.2. *Mathematical model and numerical method for DNS*

The mathematical model used here is aimed at a comprehensive representation of all relevant physical effects without any simplifying assumptions. Corresponding calculations are therefore denoted as direct numerical simulations.

The test case considered here, case D_{LDE}, applies a disturbance-flow formulation. In this formulation, a laminar flow is assumed to fulfil the steady Navier–Stokes equations and is used as a base flow. A solution is then sought only for the disturbance quantities $\boldsymbol{v}'$, $\boldsymbol{\omega}'$. Computational parameters are specified in table 1. As a base flow $\boldsymbol{v}_B$, $\boldsymbol{\omega}_B$, we take the mean flow obtained from case D_{NLDE}, which is described in Marxen (2005).

The advantage of using a disturbance formulation is a drastically reduced computational cost. First, for the disturbance formulation it is required to consider only the laminar part of the LSB (box in figure 1) in order to suppress the effect of mean flow deformation (see Marxen & Rist 2010; Marxen & Henningson 2011, for a description of this effect). This results in a shorter integration domain compared to the simulation performed to obtain the base flow. Second, to ensure laminar flow inside the integration domain, disturbances must have small amplitude only. In turn, this allows the simulations to be run with arbitrarily low spanwise resolution due to the linearity of perturbations. Finally, we found that runs in the disturbance formulation have shorter convergence times towards a periodic or steady state (see also Marxen *et al.* 2004).

2.2.1. *Boundary conditions*

The boundary conditions used in the DNS have been carefully adapted by hand in order to achieve a good matching with the experiment. This adaption included the controlled disturbance input, e.g. location and size of the disturbance strip, as well as frequency and amplitude of each forced perturbation.

In case D_{LDE}, vanishing perturbations have been prescribed at the inflow boundary x_{ifl}. Upstream of the outflow boundary at x_{ofl}, a buffer zone is placed which removes vorticity perturbations, so that velocity perturbations can leave the domain without being reflected. The domain with physically meaningful data extends to $x_{o,usable}$.

The wall-normal height of the integration domain y_{max} is chosen to be 0.1207. The flow is irrotational at this distance from the wall, and hence all vorticity components are set to zero at the upper boundary. Exponential decay of all velocity disturbances at the upper boundary is specified in case D_{LDE}. The flow field is assumed periodic in the spanwise direction. It is also assumed symmetric with respect to the plane $z = 0$.

At $y = 0$ a no-slip wall is placed. Time-harmonic perturbations are triggered via blowing and suction at the wall through zero-net-mass-flux disturbance strips. Table 2 specifies the streamwise location of the strips as well as amplitudes for each excited disturbance Fourier mode separately. The nomenclature for specifying the Fourier modes is explained in § 2.3. The wall-normal velocity vanishes everywhere at all times, except within the small strip $[x_{st}, x_{en}]$ for positive times t. The velocity distribution in

	$(1, 0)$	$(1, \pm 1)$
A_v	0.06	0.0272
Disturbance strip:	$x \in [-0.3833, -0.2093]$	$[-0.4702, -0.3833]$

TABLE 2. Forcing v-amplitudes A_v and location of the disturbance strip, case D_{LDE}.

MMAX	NMAX	KMAX + 1	IMAX	LPER
241	1738	6	1	900

TABLE 3. Resolution for test case D_{LDE}.

this strip resembles a sine-function, but with vanishing first and second x-derivatives at both the upstream and downstream ends. The forcing amplitude for the two-dimensional wave was chosen to match experimental results (see figure 10*a* below). It is initially quite large, but it quickly drops to below 1 % downstream. For the pairs of oblique waves $(1, \pm 1)$, the forcing is prescribed for each wave of the pair separately within the strip. The forced fundamental circular frequency is $\beta_0 = 2\pi/T_0 = 30.7$ and the fundamental spanwise wavenumber is $\gamma_0 = 2\pi/\lambda_z = 72$. The circular frequency $\beta_0 = 30.7$ is among the integrally most amplified frequencies according to LST, as verified *a posteriori* (see figure 6 in § 3.2).

The disturbance forcing in the DNS differs from that in the experiment. In particular, a pair of unsteady oblique waves was forced instead of a stationary spanwise-modulated disturbance. This was necessary for the best possible matching with the experiment, see Marxen *et al.* (2004, 2009) for details.

2.2.2. *Numerical method*

The method for solving the Navier–Stokes equations in vorticity–velocity formulation is based on a discretization suggested and carefully analysed by Kloker (1998), and thereafter slightly refined, extended, and optimized by many others. Further details of the numerical method and implementation can be found in Meyer, Rist & Kloker (2003).

The method uses upwind/downwind splitting (Kloker 1998) together with a compact sixth-order finite-difference scheme (Lele 1992) for downstream (*NMAX*) and wall-normal (*MMAX*) discretization. In the spanwise direction, a spectral Fourier ansatz is applied (*KMAX*+1 modes) for real (*IMAX*=1) modes. A vorticity-transport equation is advanced in time by an explicit fourth-order Runge–Kutta scheme with *LPER* time steps per fundamental period T_0. The grid resolution is specified in table 3.

2.3. *Post-processing*

Simulation and experimental results are Fourier analysed in time using available discrete time steps (for DNS equally spaced with spacing $\Delta L = LPER/25$). In the experiment, the flow field was phase averaged in order to increase the signal-to-noise ratio and thus reduce the effect of non-periodicities on the Fourier transformed results. The double Fourier transform in time and the spanwise direction yields disturbance amplitudes A and phases Φ. Transformed variables are marked by ˆ. A subscript specifies the velocity component, such as u, v, or w, for instance $A_u = |\hat{u}'^{(h,k)}|$. The notation (h, k) is used to specify modes, with h and k denoting wavenumber
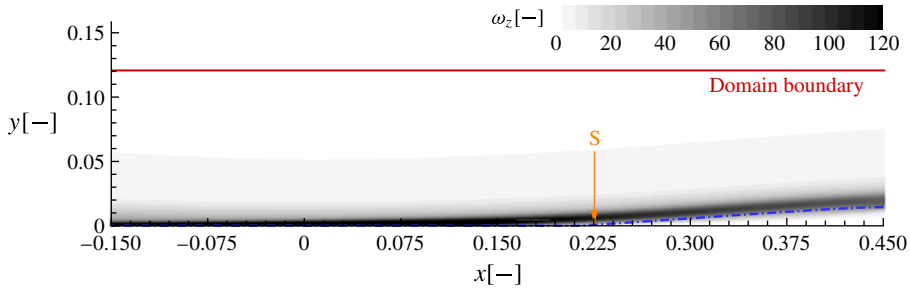
FIGURE 2. (Colour online) Contours of the time- and spanwise-averaged spanwise vorticity $\overline{\omega}_z$ from DNS together with mean dividing streamline: $\overline{\psi} = 0$ (–·–).

coefficients in time and span, respectively. In order to track downstream amplification, the maximum in y is computed.

The computations were advanced until a periodic state had been reached. Data collected during four periods of the fundamental frequency were used in the analysis of DNS data, while 20 periods have been used for measured data. The forcing frequency β_0 is the respective fundamental frequency for such an analysis.

The skin friction, c_f, in the experiment has been determined using velocity profiles. Here, we have computed the experimental skin-friction coefficient without making use of the assumption that the streamwise velocity vanishes at the wall, unlike Marxen *et al.* (2009). This leads to an improved accuracy for c_f in the region upstream of the LSB.

3. Mean flow: boundary-layer and stability properties

In this section, the time- and spanwise-averaged flow field obtained from case D_{NLDE} are described. Case D_{NLDE} is treated in more detail in Marxen (2005). This mean flow field is not only important for the theoretical analysis of small disturbances in the flow (given in § 3.2), it has also been used as the base flow for case D_{LDE}.

3.1. *Mean-flow profiles*

Contours of the spanwise vorticity ω_z are shown in figure 2, together with the mean dividing streamline $\overline{\psi} = 0$. A fairly large, yet shallow separation region is visible. Its start is marked by the point of separation S. In the experiment the point of separation was found by means of flow visualizations to lie at $x_S^{Exp} \approx 0.225$. Here and throughout this work, a nominal separation location of $x_S^{nominal} = 0.225$ is assumed and marked in some figures. This is not exactly the separation location which was found in the DNS (see figure 3*a*), but differences are small and not important as underlined by the good agreement of mean-flow profiles between measurements and DNS (figures 4 and 5).

Figure 3 shows the streamwise development of several boundary-layer parameters. We note that the measured boundary-layer thicknesses have been obtained based on actual velocities and not the pseudo-velocity (for a definition see Marxen 2005; Marxen *et al.* 2003), which could not be computed due to the sparsity of experimental data.

Figures 4 and 5 compare time- and spanwise-averaged streamwise and wall-normal velocity profiles in the laminar part of the LSB. Good matching of DNS results and measurements even for the small wall-normal velocity component (note the different
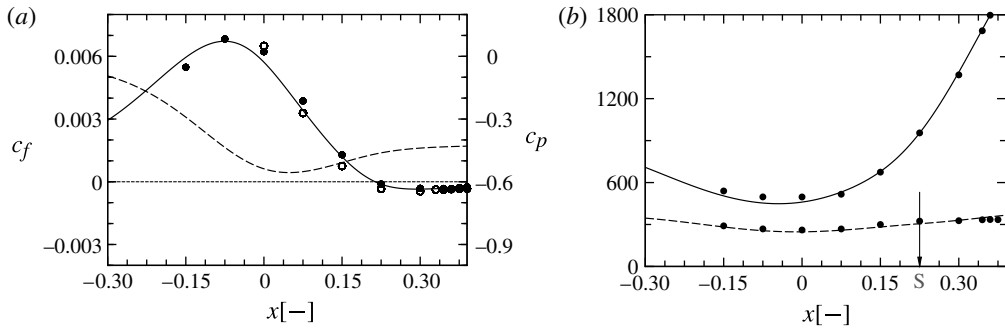
FIGURE 3. (a) Coefficients for skin friction c_f (—), surface pressure c_p (– –); (b) Reynolds numbers $Re_{\delta*}$ (—) and Re_θ (– –). Lines show DNS results and symbols show c_f derived from measurements LDA (2000) (○), LDA (2001) (●). The experimental c_f-values have been computed from wall-normal derivatives of measured profiles of the streamwise mean velocity.

scaling for u and v in the figures) suggests that the laminar boundary layer has been accurately captured by the DNS. The insets showing the reverse-flow region of the LSB confirm that a comparable amount of reverse flow exists in the DNS and in the experiment. The last x-position shown is still inside the linear disturbance region. For $x > 0.3$ differences between DNS and measurements increase for the wall-normal velocity component v in the free stream. This is due to a slightly shorter separation bubble obtained in DNS case D_{NLDE} compared to the experiment.

3.2. *Linear stability characteristics for wave-like disturbances*

Linear stability theory based on the Orr–Sommerfeld equation (see Schmid & Henningson 2001) has been applied to the laminar part of the mean flow. We use a shooting method so that at every streamwise location, a single complex eigenvalue is obtained for a prescribed real frequency and initial condition. Depending on this initial condition, the method converges to a different eigenvalue of the spectrum. The imaginary part of the eigenvalue corresponds to the streamwise amplification rate while the real part represents the wavenumber. If an eigenvalue possesses a negative imaginary part, the disturbance is amplified in x. Such an eigenvalue will be called an unstable eigenvalue.

The complete range of unsteady frequencies for the single unstable eigenvalue has been reported in Marxen *et al.* (2004), their figure 5. A non-dimensionalized version of this figure is given here as figure 6. From that figure it can be seen that the most amplified frequency, as computed by the Orr–Sommerfeld equation, is fairly constant along x. This is consistent with figure 23 in Diwan & Ramesh (2009). Marxen *et al.* (2004) have already pointed out that 'amplification starts prior to separation' (p. 140). The dent in the neutral curve, marked by a large white arrow in figure 6, is indicative of a connection between a region of viscous and inviscid instability. Such a dent, albeit much more pronounced, can be seen in figure 4 of Rist & Augustin (2006). Here, the dent is small since the region in which viscous Tollmien–Schlichting instability contributes is very small, and most of the amplification occurs due to an inviscid Kelvin–Helmholtz instability.

Inside the LSB, two-dimensional disturbances are most amplified as can be seen in figure 6(*b*). Within the streamwise interval considered here, the maximum
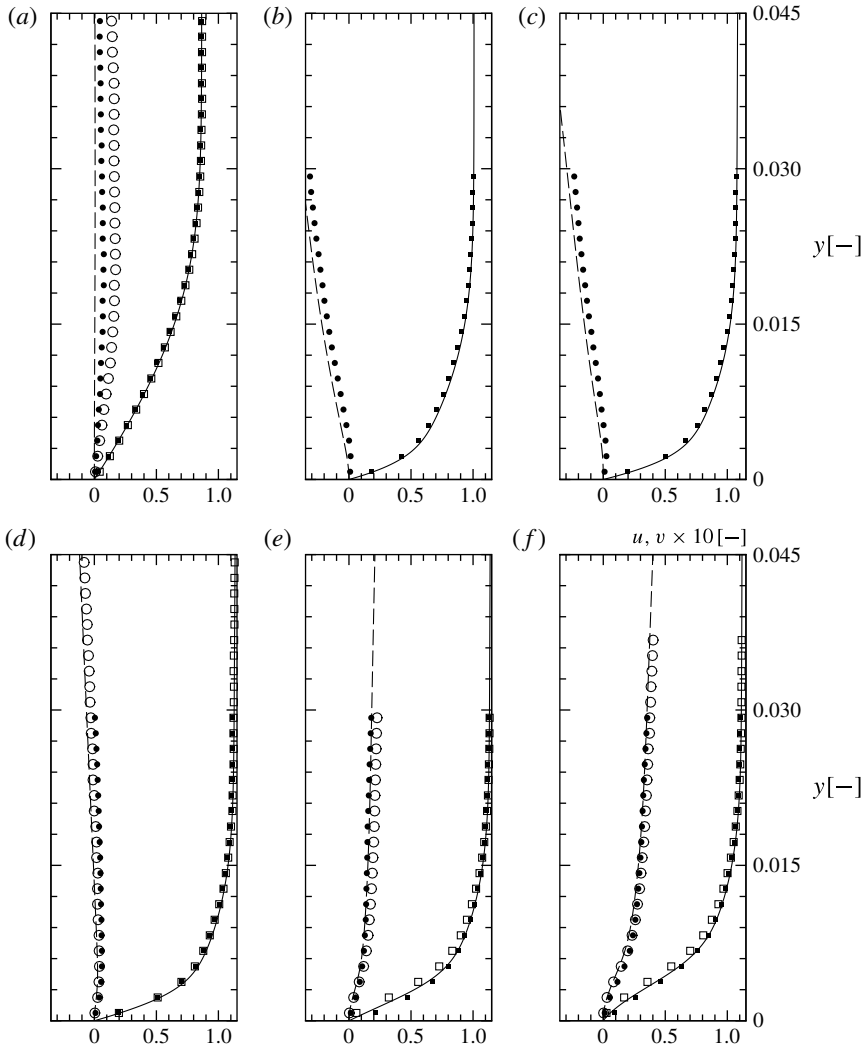
FIGURE 4. Profiles of time- and spanwise-averaged streamwise and wall-normal velocity components. Comparison of DNS (u: —, v: – –), LDA (2001) (u: ■, v: ●), and LDA (2000) (u: □, v: ○). Streamwise positions depicted are (a) $x = -0.6$, (b) $x = -0.15$; (c) $x = -0.075$; (d) $x = 0$; (e) $x = 0.075$; (f) $x = 0.15$.

reverse-flow velocity of the base flow is always below 10 % of the free-stream velocity and therefore no absolute instability can be expected according to Rist & Maucher (2002).

For transition in low-disturbance-level environments, only the least damped, or most amplified, eigenmode is usually considered (compare figure 16 in Postl *et al.* 2011). However, the linear stability properties can be characterized by an entire spectrum of eigenvalues. Apart from continuous branches of this spectrum, which will not be considered here, also a finite number of discrete eigenmodes exists (Drazin & Reid 2004). In the following we will consider also a second of these discrete eigenmodes. For a given frequency, these two discrete eigenmodes differ in their amplification rate, streamwise wavelength, and wall-normal eigenfunction.
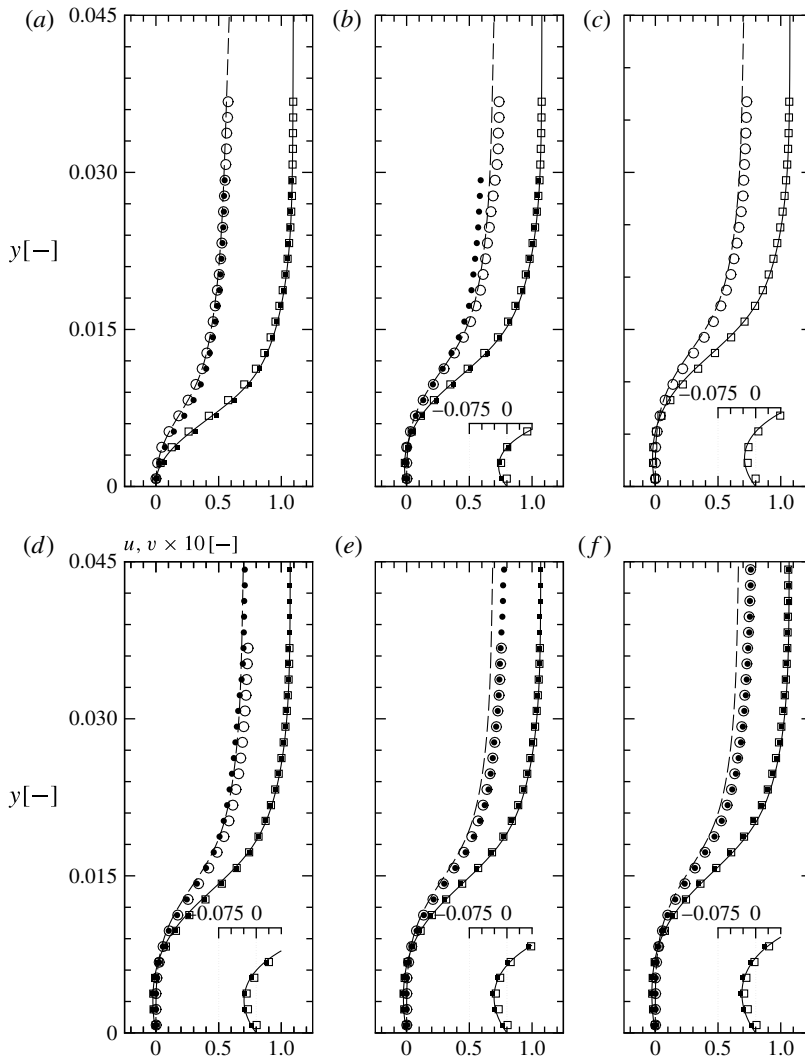
FIGURE 5. Same as figure 4 but for streamwise positions (*a*) $x = 0.225$; (*b*) $x = 0.3$, (*c*) $x = 0.33$, (*d*) $x = 0.345$, (*e*) $x = 0.36$, (*f*) $x = 0.375$. Insets show u in the reverse-flow region on a 4-times enlarged scale.

Figure 7 shows the amplification rates and wavenumbers for two-dimensional disturbances for the two different eigenmodes with the same frequency. Amplification ($\mathrm{Im}(\alpha) < 0$) sets in for the first eigenmode well before separation, approximately from $x = 0.1$ onwards. The second eigenmode possesses roughly half the wavenumber of the first one. Marxen & Henningson (2011) showed that for a separating boundary layer the amplification rate increases continuously and it is approximately proportional to the shape factor. Deeper inside the bubble (for $x > 0.3$), the amplification rate becomes almost constant (figure 7*b*), although the shear layer continues to move away from the wall. This suggests that the influence of the wall is small deeper inside the bubble. Such an effect has been observed for a generic velocity profile by
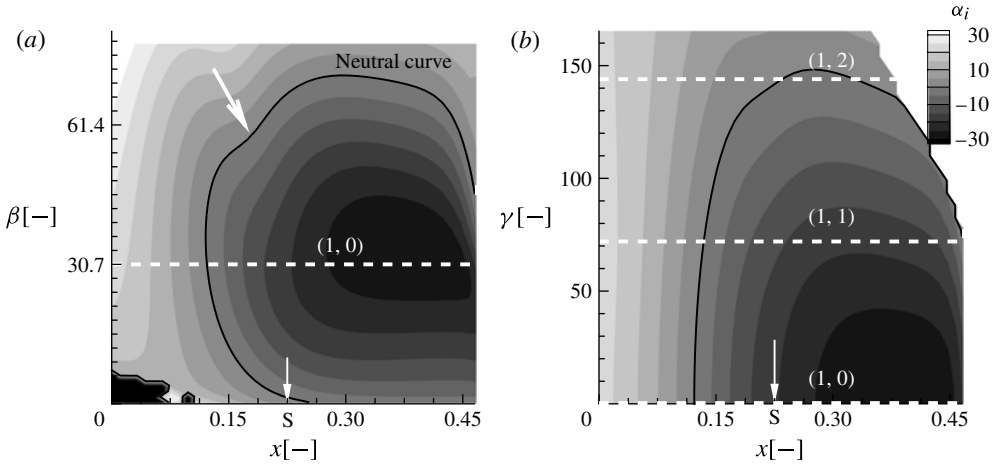
FIGURE 6. Stability diagram for the spatial case calculated from the Orr–Sommerfeld equation for: (*a*) spanwise wavenumber $\gamma = 0$; and (*b*) angular frequency $\beta = 30.7$
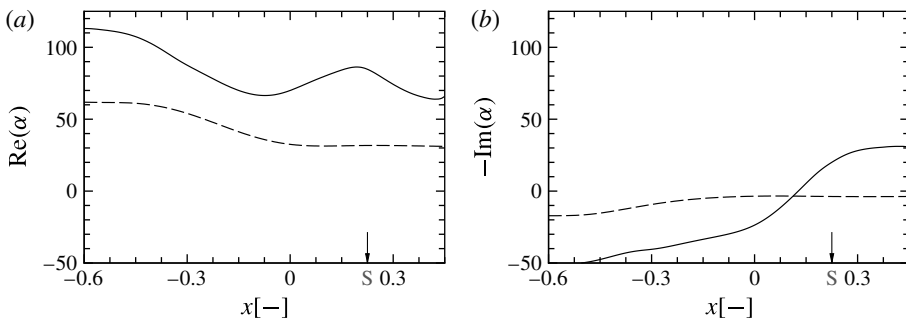

FIGURE 7. Eigenvalues from linear stability theory based on the Orr–Sommerfeld equation for two-dimensional disturbances ($\gamma = 0$) and fundamental frequency $\mathrm{Re}(\omega) = \beta_0 = 30.7$; first (—) and second (– –) eigenmode. (*a*) Streamwise wavenumber $\mathrm{Re}(\alpha)$ and (*b*) amplification rate $-\mathrm{Im}(\alpha)$.

Rist, Maucher & Wagner (1996). Upstream of the LSB, the second eigenmode exhibits a smaller $|\mathrm{Im}(\alpha)|$ compared to the first one. In this region, the first eigenmode is highly damped (figure 7*b*).

Figure 8 confirms that two-dimensional disturbances are more strongly amplified than three-dimensional disturbances at separation and inside the bubble, while the streamwise wavenumber does not differ much in this region.

In summary, our stability analysis reveals that only a single two-dimensional mode, which will be labelled the *first eigenmode*, becomes amplified in the region of APG. However, this mode is not the least-damped mode in the FPG region. Instead another mode, labelled the *second eigenmode*, is the least-damped mode in this region. Although the second eigenmode never becomes amplified, it is only moderately damped in the entire streamwise domain considered.
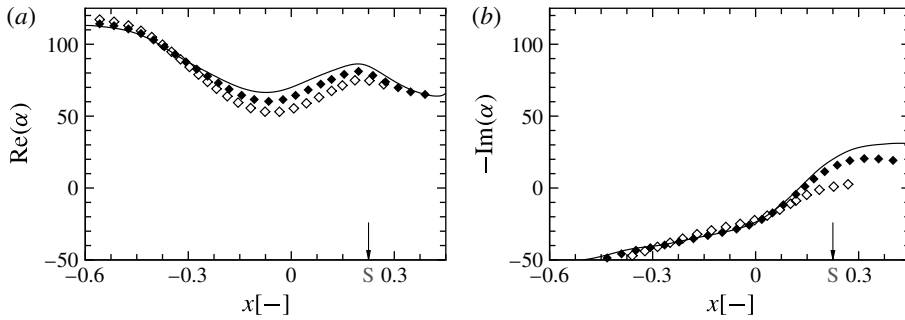
FIGURE 8. Eigenvalues from linear stability theory: (*a*) streamwise wavenumber Re(α) and (*b*) amplification rate $-$Im(α) for disturbances (first eigenmode only) with spanwise wavenumbers: —, $\gamma = 0$; $\blacklozenge$, $\gamma = 72$; $\lozenge$, $\gamma = 144$, and fundamental frequency Re(ω) = β_0 = 30.7.
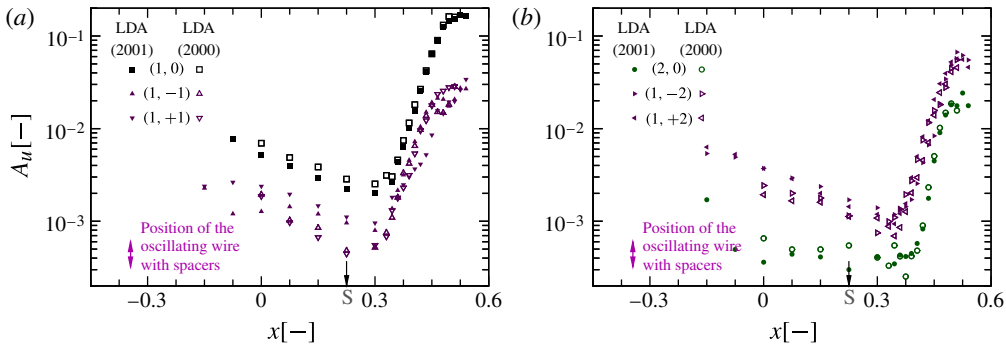

FIGURE 9. (Colour online) Measured amplification curves for the maximum (in y) streamwise velocity fluctuation $|\hat{u}'^{(h,k)}_{max}|$ for selected wavenumber coefficients h, k with $h > 0$.

4. Numerical and experimental observations of unsteady linear disturbance evolution

Marxen *et al.* (2009) reported that for the present setup, the steady mode (0, 2) is the largest disturbance in the first part of the LSB ($x \lesssim 0.42$). However, the two-dimensional disturbance of fundamental frequency, mode (1, 0), grows very strongly and eventually becomes the largest perturbation in the flow until saturation and transition sets in (figure 9). Perturbations with non-zero spanwise wavenumber and with frequencies $\beta > \beta_0$ are generally lower in amplitude.

Growing perturbations may undergo two consecutive linear stages downstream, namely first transient and then modal growth or decay. Transient growth, associated with eigenmodes of the continuous spectrum, is particularly important for stationary disturbances. This type of disturbance has been treated in detail in Marxen *et al.* (2009) for the same setup as the present one and will not be considered here. For unsteady perturbations, we found that discrete eigenmodes possess a sufficiently strong attraction so that only the second, modal stage is relevant for unsteady perturbations. Evidence for this conjecture is presented below.
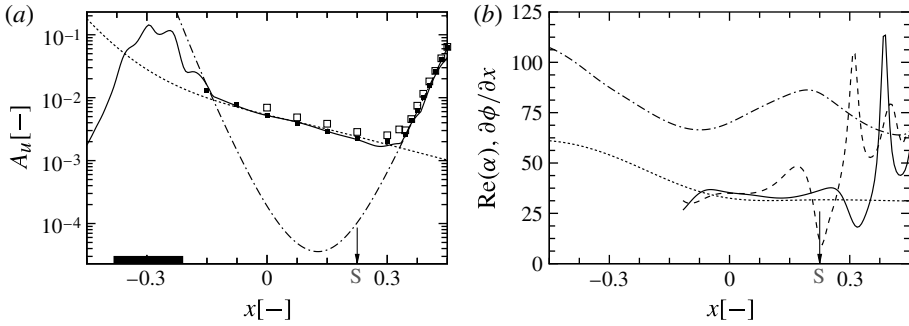
FIGURE 10. (*a*) Amplification curves for the maximum (in *y*) two-dimensional streamwise velocity fluctuation $|\hat{u}_{max}'^{(1,0)}|$. DNS, case D_{LDE} (—); LST (first eigenmode: –·–; second eigenmode: ···); measurements LDA (2001) (■), LDA (2000) (□). The disturbance strip used in the DNS is marked by a black bar. (*b*) Streamwise wavenumber for two-dimensional disturbances of fundamental frequency $\mathrm{Re}(\omega) = \beta_0 = 30.7$. LST: $\mathrm{Re}(\alpha)$ (first eigenmode: –·–; second eigenmode: ···); DNS: $\partial\Phi^{(1,0)}/\partial x$ at heights $y = 0.0063$ (- - -), $y = 0.0651$ (—).

4.1. *Experimental observations of decaying perturbations inside the separation bubble*

Figure 9 displays the remarkable feature mentioned in the introduction: the perturbation continues to decay downstream of the separation location. Further downstream, the curve representing the streamwise disturbance evolution exhibits a kink.

The harmonically oscillating wire in the experiment generates perturbations of appreciable amplitude only for the forcing frequency. All disturbances with higher frequencies are a result of nonlinear generation in the flow. Hence, linear disturbance evolution will only be considered for disturbances with the fundamental frequency $\beta_0 = 30.7$. First, we will deal with the two-dimensional disturbance $(1, 0)$ and then extend consideration to the oblique modes $(1, k)$ with $\gamma_0 = 72.0$. It is justified to consider more than one spanwise wavenumber here, since the spacers used in the experiment do not possess a sinusoidal shape but sharp edges. Hence, they may excite disturbances for a range of spanwise wavenumbers simultaneously.

4.2. *Evolution of a two-dimensional disturbance*

For the present streamwise position of the oscillating wire in the experiment $(x = -0.345)$ as well as the disturbance strip in the DNS (centred at $x = -0.2963$), we can indeed observe the least-damped eigenmode shortly after the forcing (figure 10*a*). In the FPG region, the least-damped eigenmode is the second eigenmode. Results from DNS, measurements, and LST results for the second eigenmode agree very well from $x = -0.225$ onwards, both with respect to the damping rate (figure 10*a*) as well as the streamwise wavenumber (figure 10*b*).

The disturbance forcing also excited the first eigenmode. However, this mode is strongly damped in the FPG region, and it only becomes amplified once the pressure gradient has changed to adverse. It is not until it is inside the separation bubble that this amplified first eigenmode can outgrow the second eigenmode in the case of DNS and experiment.

With the location of the disturbance strip in the DNS chosen at a similar streamwise position as in the experiment, the experimentally determined perturbation evolution can
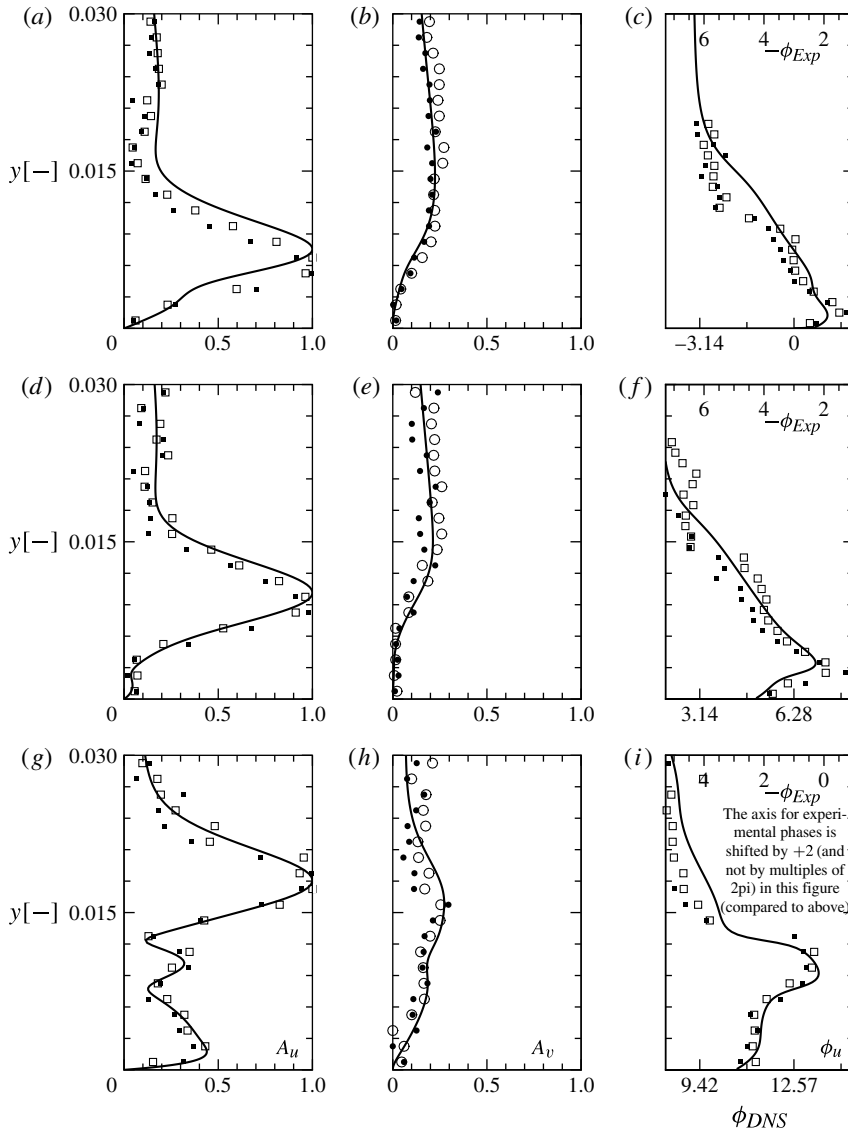
FIGURE 11. Velocity amplitudes of mode $(1, 0)$, normalized by their respective $|\hat{u}'_{max}|$ for the streamwise velocity $A_u = |\hat{u}'|$ (a, d, g), the wall-normal velocity $A_v = |\hat{v}'|$ (b, e, h), and phases for the streamwise velocity Φ_u (c, f, i) for $(a–c)$ $x = 0$; $(d–f)$ $x = 0.15$; $(g–i)$ $x = 0.3$. DNS, case D_{LDE} (—); LDA (2001) $(u$: ■, v: ●), and LDA (2000) $(u$: □, v: ○). On the *Phi* plots the top axes refer to LDA results and the bottom axes to DNS. In (i) the axis for the experimental phases is shifted by $+2$ (and not by multiples of 2π as in the other plots).

be reproduced almost perfectly in the simulation – including the position of the kink in the amplification curve.

Concerning the streamwise wavenumber (figure 10*b*), it can be seen that the take-over of the second (low wavenumber) by the first eigenmode (high wavenumber) initially takes place near the wall. This is further supported by looking at wall-normal amplitude distributions (figures 11 and 12). The second eigenmode possesses
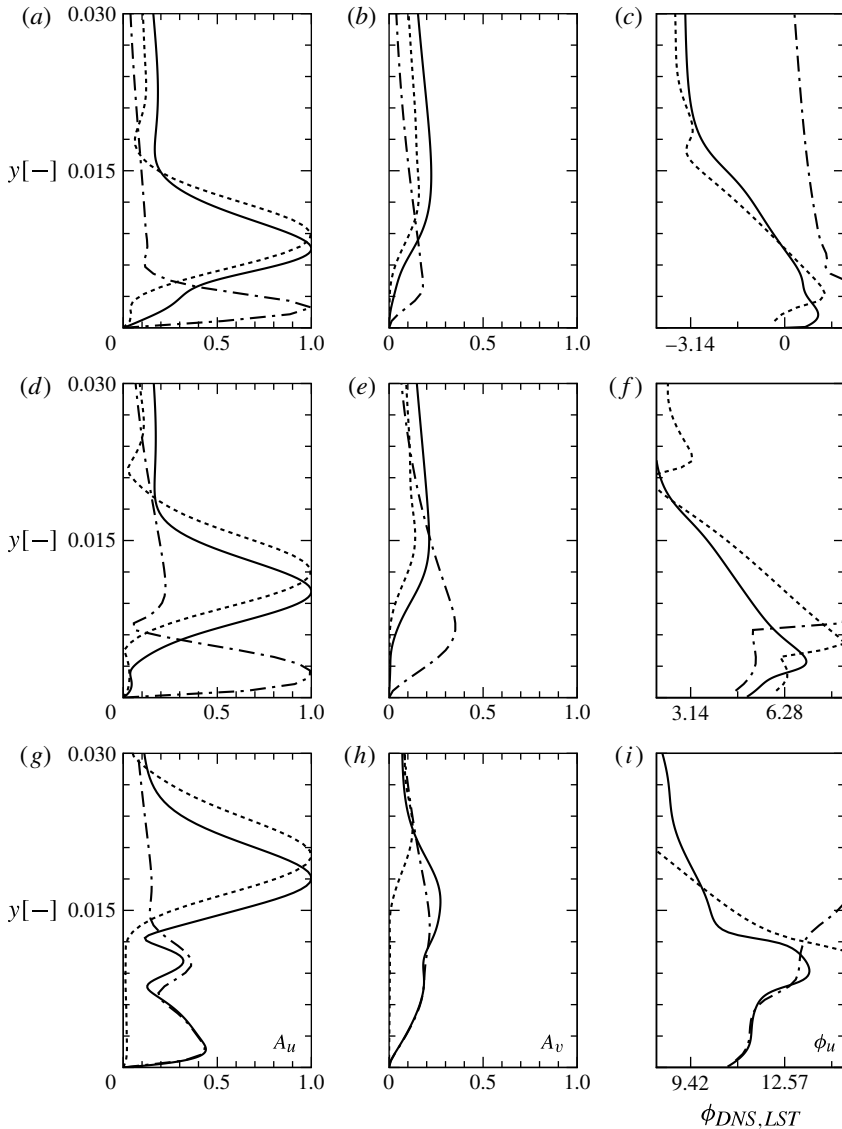
FIGURE 12. Same as figure 11, but results from DNS, case D_{LDE} (——); LST (first eigenmode:
—·—; second eigenmode: ····). (*a*–*c*) $x = 0$; (*d*–*f*) $x = 0.15$; (*g*–*i*) $x = 0.3$.

a maximum far away from the wall, while the first one shows a strong near-wall
maximum. Therefore, the stable second eigenmode can be denoted as the outer
mode and the unstable first eigenmode as the inner mode. From figure 12 we
can observe that the amplitude functions for the streamwise velocity peak closer
to the wall in DNS compared to the second linear eigenmode from LST. We do
not have an explanation for this shift, but it may well be possible that more than
one eigenmode is present, and a multimode decomposition (Tumin 2003) could
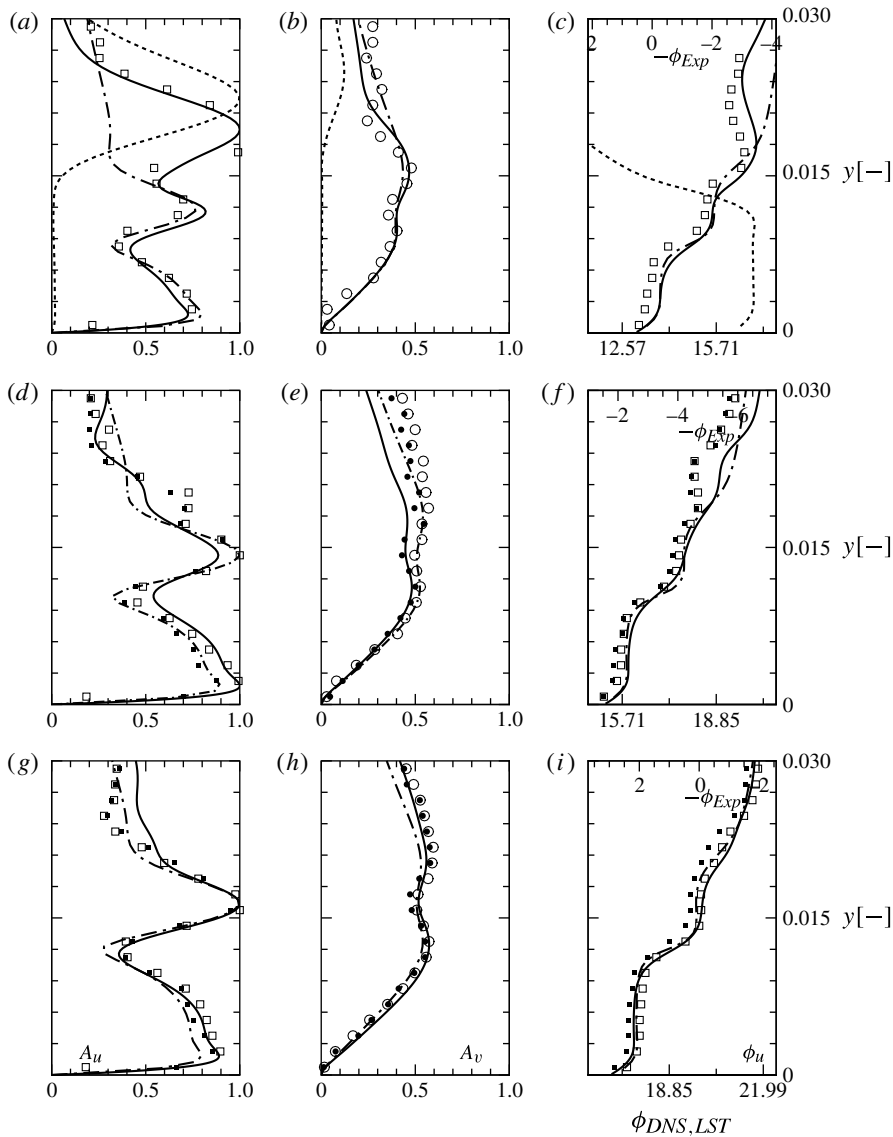provide clarification. Alternatively, non-parallel effects may be responsible for the
shift.

FIGURE 13. Same as figure 11, but for (*a–c*) $x = 0.33$; (*d–f*) $x = 0.36$, (*g–i*) $x = 0.39$. DNS, case D_{LDE} (—); LDA (2001) (*u*: ■, *v*: ●), and LDA (2000) (*u*: □, *v*: ○); LST (first eigenmode: –·–; second eigenmode: ···).

Particularly remarkable are the distributions at $x = 0.3$ (figure 12*g–i*) and $x = 0.33$ (figure 13*a–c*), where the superposition of both eigenmodes is visible. However, one should keep in mind that such a superposition depends on the different phase distributions also and is not only given by adding the two amplitude functions. At $x = 0.3$, the second eigenmode dominates the amplitude distribution away from the wall, while the first eigenmode dominates the near-wall region. In the figures, the scaling of the first-eigenmode LST eigenfunction at the two positions $x = 0.3$ (figure 12*g*) and $x = 0.33$ (figure 13*g*) was adapted, i.e. normalized by a properly chosen $C|\hat{u}'_{max}|$ ($C > 0$) instead of just $|\hat{u}'_{max}|$.
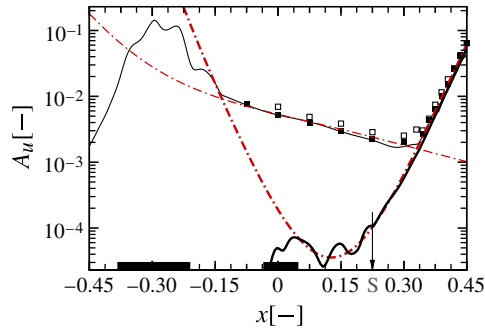
FIGURE 14. (Colour online) Amplification curves for the maximum (in y) streamwise velocity fluctuation $|\hat{u}'^{(h,k)}_{max}|$, DNS results for cases D_{LDE} (thin lines) and D_{NLDE} (thick lines). mode $(1, 0)$ —, LDA (2001) (■), LDA (2000) (□), and LST (–·–), thick line: first eigenmode and thin line: second eigenmode.

It has long been known that eigenvalues from LST agree with measurements for an LSB, see for instance figure 20 in Gaster (1967). However, eigenfunctions also agree very well between LST on the one hand and DNS or experiment on the other, as can be seen in figure 13(*d–i*). Such a good agreement has been previously observed for a backward-facing step, see figure 10 in Boiko *et al.* (2011).

The phase from the DNS given in figures 12 and 13 increases from one x-location to the next with respect to a reference phase: this reference phase, where $\Phi = 0$, is located at maximum A_u for $x = 0$. A fixed reference phase has also been chosen for the measured data. However, this reference phase is different for $x = 0, 0.15$ so that experimental phase distributions appear as shifted by $\Delta\Phi = -2$ at $x = 0, 0.15$ compared to the other x-locations. The reason for our adjustment of the reference phase is that the phase difference between the two different eigenmodes present in the data is slightly different in the experiment and in the DNS.

Deeper inside the LSB, the unstable eigenmode becomes dominating in the DNS case D_{LDE}. We conjecture that in the DNS, it may be sufficient to excite this first eigenmode only, e.g. with a disturbance strip placed at the location of pressure minimum ($x = 0$) or even closer to the LSB to obtain the same transition process. Marxen *et al.* (2004, 2003) introduced their perturbations at these locations. The validity of this hypothesis will be verified now by comparing the evolution of mode $(1, 0)$ between the case D_{LDE} (here) and case D_{NLDE} (Marxen 2005).

Figure 14 shows that the evolution of mode $(1, 0)$ deeper inside the LSB for $x > 0.36$ for the two different cases is indistinguishable, proving the conjecture. Hence, one need excite only the amplified first eigenmode by relocating the disturbance strip to the region around the pressure minimum ($x = 0$) as in D_{NLDE} without altering the transition dynamics deeper inside the bubble.

Even for cases where no laminar base flow is obtainable if the entire LSB is contained in the computational domain, a disturbance formulation is applicable for the part of the flow containing only small amplitude, i.e. linear perturbations, as has been shown by a comparison of both formulations. The application of a disturbance formulation results in considerable savings of computational time compared to a run in total-flow formulation due to a faster convergence towards a (quasi-) periodic state and lower resolution. Such an approach allows the separation of the flapping motion of the entire bubble from the shear-layer instability. However, application of the disturbance
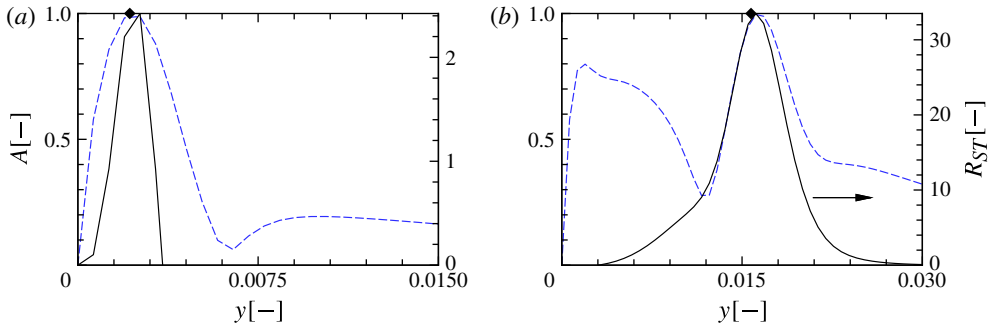
FIGURE 15. (Colour online) Eigenfunctions for the streamwise velocity from LST for the unstable first eigenmode (- - -) at (*a*) $x = 0.1125$ and (*b*) $x = 0.39$, together with the corresponding Reynolds stress term $R_{ST}^{(1,0)}$ (—, right-hand axis). The location of the inflection point y_{IP} of the mean-flow profile is marked by ◆.

formulation inevitably requires the knowledge of the transition mechanism so that the correct type and number of perturbations can be forced that guarantee the same transition location.

4.3. *Disturbance growth mechanisms for the first eigenmode*

As mentioned in the introduction, two different types of instability may lead to disturbance amplification: a viscous Tollmien–Schlichting mechanism and an inviscid Kelvin–Helmholtz mechanism. The type of instability will now be determined. According to a definition introduced in Rist & Maucher (2002), a Tollmien–Schlichting wave should possess an amplitude maximum near the wall, while a Kelvin–Helmholtz instability wave exhibits a maximum in the shear layer. In classifying their disturbance, Marxen *et al.* (2003) followed this definition based on the relative strength of the first and second wall-normal maximum of the streamwise disturbance velocity. According to this classification, we would have a TS wave up to $x \approx 0.3$ (figure 12*g*) and a KH wave further downstream (figure 13).

Here, we take a different viewpoint and consider the actual disturbance energy production mechanism in order to determine the type of instability active at different locations in the separating boundary layer. Hence, we look at the Reynolds stress term $R_{ST} = A_u A_v \cos(\Phi_u - \Phi_v) \partial u_B / \partial y$, which is depicted in figure 15. The location of maximum R_{ST} will be denoted by $y_{max,EP}$.

An unstable eigenmode is first seen at $x \approx 0.1125$ (figure 6). At this location, the eigenfunction is very similar to that observed in a Falkner–Skan boundary layer. The location of the inflection point of the base-flow profile will be labelled y_{IP}. Following Diwan & Ramesh (2009), we consider the ratio $y_{IP}/y_{max,EP}$ in order to determine whether we have a TS or a KH instability. If only a TS instability is active, this ratio should be zero, while for a pure KH instability it should assume a value of one.

At the onset of instability $x = 0.1125$, the ratio $y_{IP}/y_{max,EP} \approx 0.82$ (figure 15*a*), suggesting that a TS mechanism contributes to the instability. However, this ratio is not very small and a KH mechanism is already contributing to the instability. This is consistent with the discussion of the stability diagram in § 3.2, in which we saw a small dent only at the onset of instability. Inside the bubble at $x = 0.39$ (figure 15*b*), the ratio increases to $y_{IP}/y_{max,EP} \approx 0.98$, indicating a pure KH instability.
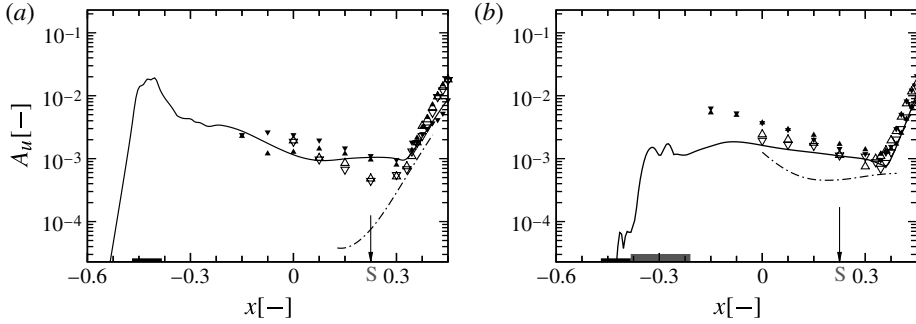
FIGURE 16. Amplification curves for the maximum (in y) streamwise velocity fluctuation $|\hat{u}_{max}'^{(1,k)}|$. DNS D_{LDE} (—); LST (–·–); measurements LDA (2001) ($k < 0$: ▲, $k > 0$: ▼), LDA (2000) ($k < 0$: △, $k > 0$: ▽). Spanwise modes with: (*a*) $k = \pm 1$; and (*b*) $k = \pm 2$.

4.4. *Evolution of oblique disturbances*

According to the linear stability analysis of § 3.2 only the perturbation with the fundamental spanwise wavelength, i.e. mode $(1, \pm 1)$, possesses sufficiently large growth rates to result in a significant region of linear amplification. Existence of such a region is confirmed by the present results (figure 16*a*, $x > 0.3$). The perturbation $(1, \pm 1)$ undergoes the same type of evolution as the previously discussed mode $(1, 0)$: a second-eigenmode decay in the FPG region as well as in the first part of the APG region is followed by a first-eigenmode amplification inside the LSB.

Again, agreement between experimental amplitude functions and DNS results is good in the region of linear instability (figure 17), even though the scatter in the measurements is slightly larger now. The position of the wall-normal maximum agrees well (figure 17), and a close agreement of DNS and LST results for the first eigenmode can be seen in the region close to the wall for $x > 0.36$. It is remarkable that asymmetries are already visible in the experiment at these early stages, i.e. a difference between the $k = +1$ and $k = -1$ mode, in particular for $x \gtrsim 0.37$ in both figures 16 and 17. A similar observation was made for the steady disturbance mode $(0, 2)$ in Marxen *et al.* (2009).

Evolution of mode $(1, \pm 2)$ does not favourably compare with the first eigenmode from LST (figure 16*b*). Whereas LST predicts only weak growth for the first eigenmode this disturbance shows the same kink in the amplification curve followed by a strong growth. Such a behaviour is a result of nonlinear generation, caused by a large-amplitude mode $(0, 2)$ together with the linearly amplified mode $(1, 0)$, as shown in Marxen *et al.* (2004). It is not surprising to see that, unlike mode $(1, \pm 1)$, this mode does not match eigenfunctions from LST (figure 18, $x = 0.3$). Further downstream ($x \geqslant 0.39$), it looks remarkably similar to amplitude functions for mode $(1, \pm 1)$, despite the different growth mechanisms.

4.5. *Disturbance excitation*

As explained in § 2.2.1, the disturbance input in the numerical simulations is given by the excitation of Fourier modes $(1, 0)$ and $(1, \pm 1)$ via blowing and suction at the wall. The excitation of only these two types of disturbances can be viewed as a simple model of the experimental disturbance excitation by means of spacers and the oscillating wire. The linear nature of the disturbances justifies applying a disturbance formulation in the simulation for case D_{LDE}.
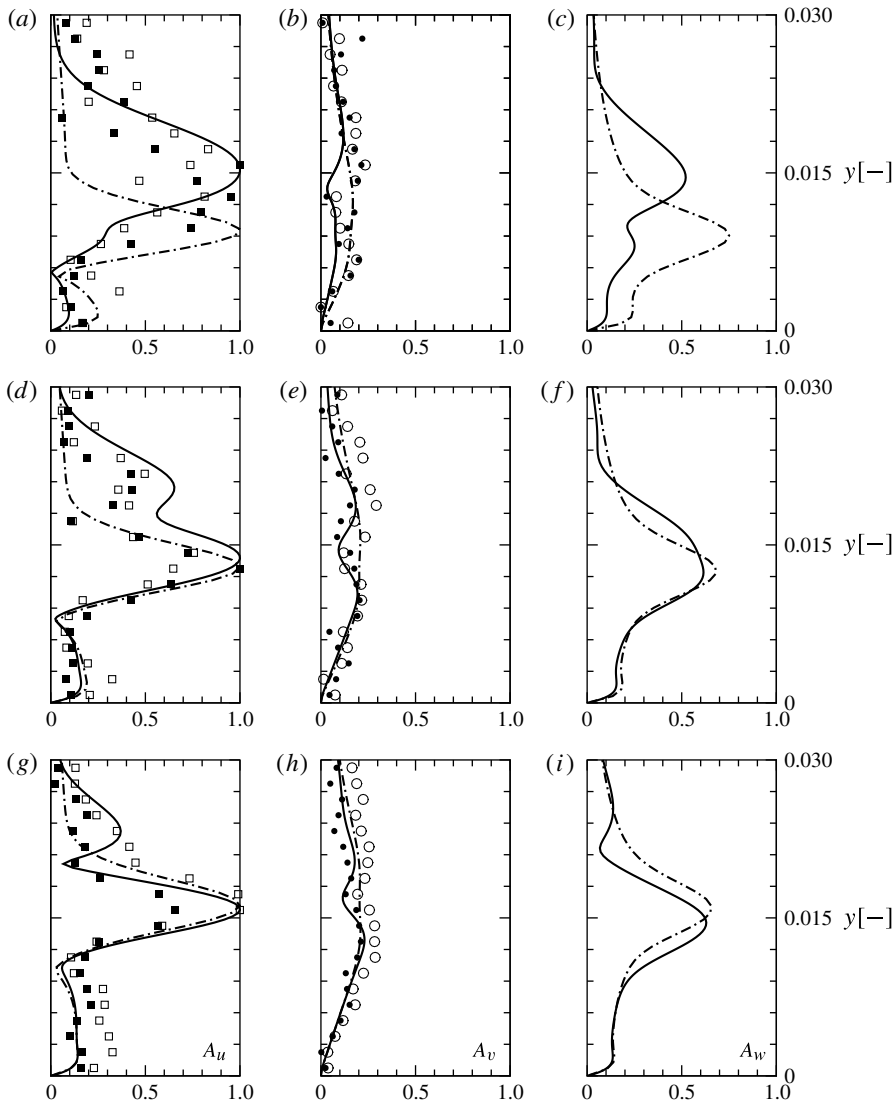
FIGURE 17. Velocity amplitudes of mode $(1, \pm 1)$, normalized by their respective $|\hat{u}'_{max}|$ for the streamwise velocity $A_u = |\hat{u}'|$ (a, d, g), the wall-normal velocity $A_v = |\hat{v}'|$ (b, e, h), and the spanwise velocity $A_w = |\hat{w}'|$ (c, f, i) for $(a–c)$ $x = 0.3$, $(d–f)$ $x = 0.345$; $(g–i)$ $x = 0.39$. DNS D_{LDE} (—); LDA (2001) (+ mode: u, ■; v, •; − mode: u, □; v, ○); LST (first eigenmode: –·–).

It is not possible to excite a single eigenmode. Rather, *all* eigenmodes of the spectrum with the respective frequency (and spanwise wavenumber) may be excited (Ashpis & Reshotko 1990), though with different initial amplitudes, respectively. The details of this forcing are responsible for the initial amplitudes of the respective eigenmodes. The process of conversion of external forcing (in the case of our experiment the oscillating wire and in case of our DNS the wall blowing/suction) into boundary-layer disturbances is called the receptivity process (Saric, Reed & Kerschen 2002). Relevant details for this process include the length and streamwise position of the disturbance strip in the numerical simulation, or the wall distance, thickness, and
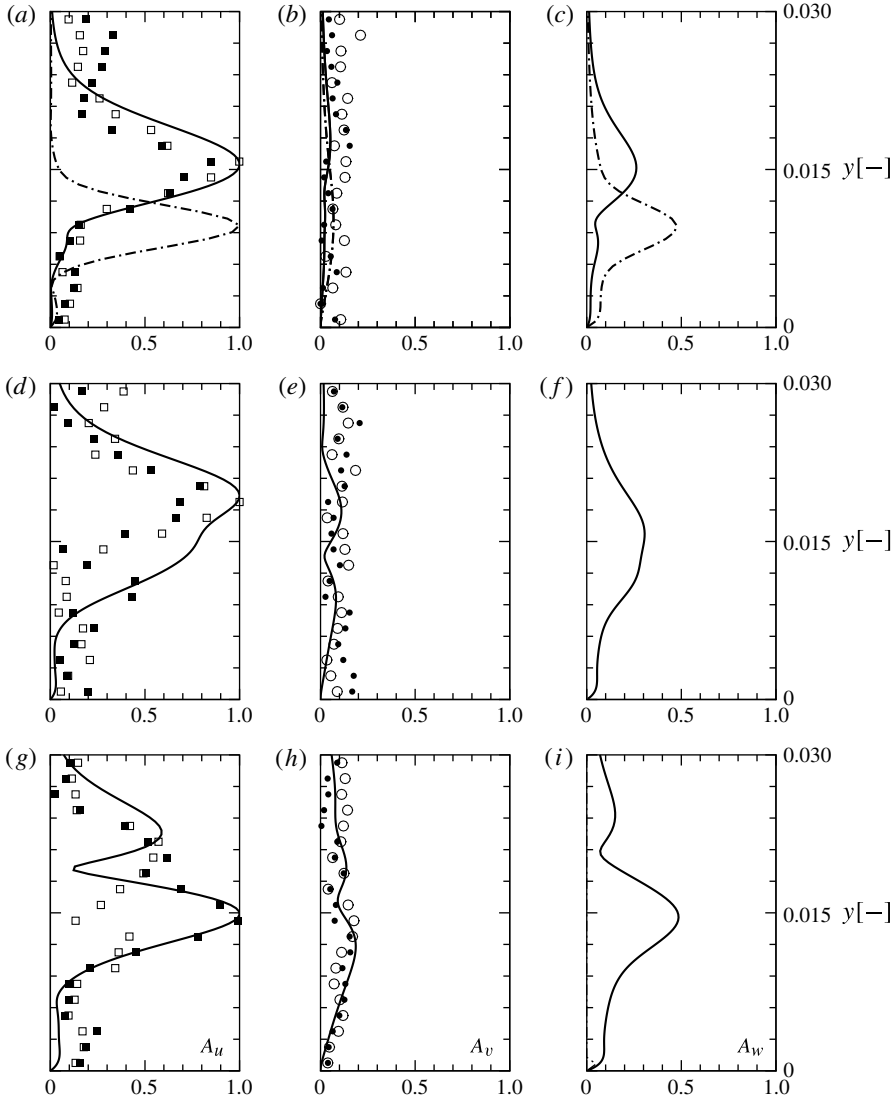
FIGURE 18. Velocity amplitudes of mode $(1, \pm2)$, normalized by their respective $|\hat{u}'_{max}|$ for the streamwise velocity $A_u = |\hat{u}'|$ (a, d, g), the wall-normal velocity $A_v = |\hat{v}'|$ (b, e, h), and the spanwise velocity $A_w = |\hat{w}'|$ (c, f, i) for $(a–c)$ $x = 0.3$; $(d–f)$ $x = 0.345$; $(g–i)$ $x = 0.39$. DNS D_{LDE} (—); LDA (2001) ($+$ mode: u, ■; v, ●; $-$ mode: u, □; v, ○); LST (first eigenmode: –·–).

streamwise position of the wire in the experiment. If one of the excited eigenmodes is significantly less damped (or more amplified) than all others, we will eventually observe only this eigenmode in the flow ('far-field response'). If we consider only the immediate vicinity of the forcing location ('near-field response') we may see a superposition resulting from a mixture of many eigenmodes. Transient growth is commonly attributed to the evolution of a mixture, or sum of, non-normal eigenmodes, which may be damped individually (Schmid & Henningson 2001).

The disturbance strip in the numerical computation has to be adjusted separately for each spanwise wavenumber of the perturbation. By means of a proper choice

of its respective length and position with respect to the base flow and to other perturbations, close agreement with experimental results even for different two-dimensional eigenmodes with the same frequency could be achieved. It is therefore possible to adjust the length of the disturbance strip in a way that the same relation of both eigenmodes is obtained in the DNS as in the experiment. The way disturbances were forced in the DNS can hence serve as a fairly good model for the oscillating wire in the experiment in conjunction with the spacers – no true modelling of the shape of the experimental disturbance devices is required.

5. Conclusions

We have performed a detailed investigation of small-amplitude disturbances in a separating laminar boundary layer. A linear stability analysis has focused on two local eigenmodes. Only one of these eigenmodes eventually becomes unstable deeper inside the bubble, while the other one is always stable. The amplitude function for the streamwise velocity of the stable eigenmode peaks at the edge of the boundary or at the outer edge of the shear layer and can therefore be called the outer mode. The unstable mode possesses maxima at the wall or at the location of the shear layer and we call it the inner mode. The value of the streamwise wavenumber for the unstable inner mode was approximately two times that of the stable outer mode.

Comparing results from direct numerical simulation and measurements with the theoretically determined properties of these two eigenmodes revealed that both eigenmodes are present in the early laminar part of a laminar separation bubble. The outer mode appears due to a strong acceleration region upstream of the bubble, which strongly damps the inner mode while only a moderate damping is observed for the outer mode. The inner mode becomes unstable in the APG region and eventually overtakes the outer mode in amplitude only inside the bubble, leading to breakdown to turbulence. This observation provides one possible explanation for the decay of perturbations often seen in the laminar part of an LSB if the boundary layer was subject to a strong acceleration upstream.

Hence, observations of decaying disturbances in the laminar part of an LSB do not constitute sufficient evidence that the flow is initially stable and becomes unstable only when the shear layer has strongly detached. Instead, the possible occurrence of two different eigenmodes in the first part of the LSB underlines the need for knowledge of disturbance details, i.e. spanwise and streamwise wavenumbers as well as the frequency, for a correct interpretation of processes in the flow. Such an interpretation may be essential for flow-control applications such as the one applied in Rist & Augustin (2006). If this information is not available, linear stability theory may aid in determining the most relevant modes *a posteriori* via a comparison with the observed disturbance amplification. The technique of multimode decomposition (Tumin 2003) would provide an even more general approach to determine the number and role of the eigenmodes involved.

At the onset of instability, both a viscous Tollmien–Schlichting and an inviscid Kelvin–Helmholtz instability seem to contribute to disturbance energy production for the inner mode, while inside the bubble we observe a pure inviscid instability. This observation suggests that the viscous mechanism is important only when the bubble is very small, when only a moderately strong acceleration precedes the APG, or when the boundary-layer Reynolds number upstream of the bubble is already sufficiently high (but not too high). In all these mentioned cases we can expect a viscosity-driven

– or at least viscosity-enhanced – boundary-layer instability upstream of the bubble already.

We found that pairs of oblique waves with moderately large spanwise wavenumbers behave in the same way as two-dimensional waves. This suggests that cases of oblique breakdown, which have been investigated only in numerical simulations, may also occur in practice. Subharmonic disturbances have been found to play a role for boundary layers subject to an APG (Corke & Gruber 1996), but they do not appear in DNS case D_{LDE}. In DNS case D_{NLDE}, which was run to obtain the base flow, they appear during nonlinear breakdown for $x > 0.45$, but their amplitude remains well below 10^{-3} in the part of the LSB considered here.

Finally, we have demonstrated that it is meaningful to use a disturbance formulation for the analysis of flow in a laminar separation bubble for unsteady waves also, similar to what has been shown earlier by Marxen *et al.* (2009) for steady perturbations. This advantage of the disturbance formulation can be exploited for parametrical variations of the disturbance input, necessary to eventually reproduce the disturbance evolution in the experiment as closely as possible. Our findings regarding convectively amplified disturbances for a separation bubble complement those in which such disturbances could not be found, see for instance Spalart & Strelets (2000) and Jones *et al.* (2008).

Acknowledgements

REFERENCES

ASHPIS, D. E. & RESHOTKO, E. 1990 The vibrating ribbon problem revisited. *J. Fluid Mech.* **213**, 531–547.

BOIKO, A., DOVGAL, A., HEIN, S. & HENNING, A. 2011 Particle image velocimetry of a low-Reynolds-number separation bubble. *Exp. Fluids* **50**, 13–21.

CORKE, T. C. & GRUBER, S. 1996 Resonant growth of three-dimensional modes in Falkner–Skan boundary layers with adverse pressure gradients. *J. Fluid Mech.* **320**, 211–233.

DIWAN, S. S. & RAMESH, O. N. 2009 On the origin of the inflectional instability of a laminar separation bubble. *J. Fluid Mech.* **629**, 263–298.

DRAZIN, P. G. & REID, W. H. 2004 *Hydrodynamic Stability*, 2nd edn. Cambridge University Press.

FEDOROV, A. & TUMIN, A. 2011 High-speed boundary-layer instability: old terminology and a new framework. *AIAA J.* **49** (8), 1647–1657.

GASTER, M. 1967 The Structure and Behaviour of Separation Bubbles, Aeronautical Research Council, Reports and Memoranda No. 3595, London.

GRUBER, K., BESTEK, H. & FASEL, H. 1987 Interaction between a Tollmien–Schlichting wave and a laminar separation bubble. *AIAA Paper* 1987–1256.

HÄGGMARK, C. P., BAKCHINOV, A. A. & ALFREDSSON, P. H. 2000 Experiments on a two-dimensional laminar separation bubble. *Phil. Trans. R. Soc. Lond.* A **358**, 3193–3205.

HAIN, R., KÄHLER, C. J. & RADESPIEL, R. 2009 Dynamics of laminar separation bubbles at low-Reynolds-number aerofoils. *J. Fluid Mech.* **630**, 129–153.

JONES, L. E., SANDBERG, R. D. & SANDHAM, N. D. 2008 Direct numerical simulations of forced and unforced separation bubbles on an airfoil at incidence. *J. Fluid Mech.* **602**, 175–207.

KACHANOV, Y. S. & LEVCHENKO, V. Y. 1984 The resonant interaction of disturbances at laminar-turbulent transition in a boundary layer. *J. Fluid Mech.* **138**, 209–247.

KLEBANOFF, P. S., TIDSTROM, K. D. & SARGENT, L. M. 1962 The three-dimensional nature of boundary-layer instability. *J. Fluid Mech.* **12**, 1–34.

KLOKER, M. 1998 A robust high-resolution split-type compact FD scheme for spatial direct numerical simulation of boundary-layer transition. *Appl. Sci. Res.* **59**, 353–377.

KOTAPATI, R. B., MITTAL, R., MARXEN, O., HAM, F., YOU, D. & CATTAFESTA III, L. N. 2010 Nonlinear dynamics and synthetic-jet-based control of a canonical separated flow. *J. Fluid Mech.* **654**, 65–97.

LANG, M., RIST, U. & WAGNER, S. 2004 Investigations on controlled transition development in a laminar separation bubble by means of LDA and PIV. *Exp. Fluids* **36**, 43–52.

LELE, S. K. 1992 Compact finite difference schemes with spectral-like resolution. *J. Comput. Phys.* **103**, 16–42.

LEVIN, O., CHERNORAY, V. G., LÖFDAHL, L. & HENNINGSON, D. S. 2005 A study of the Blasius wall jet. *J. Fluid Mech.* **539**, 313–347.

MACK, L. M. 1975 Linear stability theory and the problem of supersonic boundary-layer transition. *AIAA J.* **13** (3), 278–2285.

MARXEN, O. 2005 Numerical studies of physical effects related to the controlled transition process in laminar separation bubbles. Dissertation, Universität Stuttgart.

MARXEN, O. & HENNINGSON, D. S. 2011 The effect of small-amplitude convective disturbances on the size and bursting of a laminar separation bubble. *J. Fluid Mech.* **671**, 1–33.

MARXEN, O., LANG, M., RIST, U., LEVIN, O. & HENNINGSON, D. S. 2009 Mechanisms for spatial steady three-dimensional disturbance growth in a non-parallel and separating boundary layer. *J. Fluid Mech.* **634**, 165–189.

MARXEN, O., LANG, M., RIST, U. & WAGNER, S. 2003 A combined experimental/numerical study of unsteady phenomena in a laminar separation bubble. *Flow Turbul. Combust.* **71**, 133–146.

MARXEN, O. & RIST, U. 2010 Mean flow deformation in a laminar separation bubble: separation and stability characteristics. *J. Fluid Mech.* **660**, 37–54.

MARXEN, O., RIST, U. & HENNINGSON, D. S. 2006 Steady three-dimensional streaks and their optimal growth in a laminar separation bubble. In *New Results in Numerical and Experimental Fluid Mechanics V* (ed. H. J. Rath, C. Holze, H.-J. Heinemann, R. Henke & H. Hönlinger), *Notes on Numerical Fluid Mechanics and Multidisciplinary Design (NNFM),* vol. 92, Springer, Contributions to the *14th STAB/DGLR Symposium, Nov. 16–18, 2004, Bremen, Germany.*

MARXEN, O., RIST, U. & WAGNER, S. 2004 Effect of spanwise-modulated disturbances on transition in a separated boundary layer. *AIAA J.* **42** (5), 937–944.

MAUCHER, U., RIST, U. & WAGNER, S. 2000 Refined interaction method for direct numerical simulation of transition in separation bubbles. *AIAA J.* **38** (8), 1385–1393.

MEYER, D., RIST, U. & KLOKER, M. 2003 Investigation of the flow randomization process in a transitional boundary layer. In *High Performance Computing in Science and Engineering'03* (ed. E. Krause & W. Jäger), *Transactions of the HLRS 2003*, pp. 239–253. Springer.

POSTL, D., BALZER, W. & FASEL, H. F. 2011 Control of laminar separation using pulsed vortex generator jets: direct numerical simulations. *J. Fluid Mech.* **676**, 81–109.

RIST, U. & AUGUSTIN, K. 2006 Control of laminar separation bubbles using instability waves. *AIAA J.* **44** (10), 2217–2223.

RIST, U. & MAUCHER, U. 2002 Investigations of time-growing instabilities in laminar separation bubbles. *Eur. J. Mech. (B/Fluids)* **21**, 495–509.

RIST, U., MAUCHER, U. & WAGNER, S. 1996 Direct numerical simulation of some fundamental problems related to transition in laminar separation bubbles. In *Computational Fluid Dynamics'96* (ed. J.-A. Désidéri, C. Hirsch, P. Le Tallec, M. Pandolfi & J. Périaux), pp. 319–325. John Wiley & Sons.

ROBERTS, S. K. & YARAS, M. I. 2006 Large-eddy simulation of transition in a separation bubble. *Trans. ASME: J. Fluids Engng* **128**, 232–238.

SANDHAM, N. D. 2008 Transitional separation bubbles and unsteady aspects of aerofoil stall. *Aeronaut. J.* **112** (1133), 395–404.

SARIC, W. S., REED, H. L. & KERSCHEN, E. J. 2002 Boundary-layer receptivity to free stream disturbances. *Annu. Rev. Fluid Mech.* **34**, 291–319.

SCHLICHTING, H. 1933 Zur Entstehung der Turbulenz bei der Plattenströmung. In *Nachr. Ges. Wiss. Göttingen, Math.-Phys. Klasse*, pp. 181–208, also *Z. Angew. Math. Mech.* **13** (3), 171–174.

SCHMID, P. J. & HENNINGSON, D. S. 2001 *Stability and Transition in Shear Flows*, 1st edn. Springer.

SPALART, P. R. & STRELETS, M. K. 2000 Mechanisms of transition and heat transfer in a separation bubble. *J. Fluid Mech.* **403**, 329–349.

TOLLMIEN, W. 1929 Über die Entstehung der Turbulenz. 1. Mitteilung, pp. 21–44. English translation: The production of turbulence. *NACA TM* 609 (1931).

TUMIN, A. 2003 Multimode decomposition of spatially growing perturbations in a two-dimensional boundary layer. *Phys. Fluids* **15** (9), 2525–2540.

TUMIN, A. & AIZATULIN, L. 1997 Instability and receptivity of laminar wall jets. *Theor. Comput. Fluid Dyn.* **9**, 33–45.

WATMUFF, J. H. 1999 Evolution of a wave packet into vortex loops in a laminar separation bubble. *J. Fluid Mech.* **397**, 119–169.

YARUSEVYCH, S., SULLIVAN, P. E. & KAWALL, J. G. 2009 On vortex shedding from an airofoil in low-Reynolds-number flows. *J. Fluid Mech.* **632**, 245–271.